Phase-field simulation of martensitic transformation with different conditions in inhomogeneous polycrystals

H. Xiang [1,*], W. Van Paepegem [2] and L.A.I. Kestens [1,*]

[1] Department of Electromechanical, Systems and Metal Engineering, Faculty of Engineering and Architecture, Ghent University, Tech-Lane Ghent Science Park-Campus A, Technologiepark Zwijnaarde 46, B-9052; Hao.Xiang@UGent.be(H. Xiang); Leo.Kestens@UGent.be(L. Kestens)

[2] Department of Materials, Textiles and Chemical Engineering (MaTCh), Faculty of Engineering and Architecture, Ghent University, Tech-Lane Ghent Science Park-Campus A, Technologiepark Zwijnaarde 46, B-9052; Wim.VanPaepegem@UGent.be (W. Van Paepegem)

* Correspondence: Hao.Xiang@UGent.be(H. Xiang); Leo.Kestens@UGent.be(L. Kestens)

Abstract: The microstructure evolution of Ti64 has been simulated to investigate the effect of different factors on the martensitic transformation (MT) in an elastically homogeneous system within a single parent grain by many researchers. In the present case the MT in a polycrystalline aggregate is considered taking into consideration the inhomogeneous elasticity of different orientations. In the present work, the phase- field modelling (PFM) is employed to study the microstructure evolution of nucleation and growth in different conditions during MT for Ti-6Al-4V polycrystalline alloy in two dimensions, including external tension/compression loading, with and without plastic deformation and strain hardening. Results indicate that the grain boundaries are the prior sites for nucleation of martensite plates, and the external loading and plastic deformation can influence the microstructure to a large degree. It can be concluded that the change of elastic strain and stress in the simulated system, including the applied loading, strain relaxation at grain boundaries and plastic deformation are important features during MT. The martensitic product structure can be predicted with the current polycrystalline phase field model.

Keywords: Ti-6Al-4V; martensitic transformation; phase field simulation; polycrystal; inhomogeneous elasticity

1. Introduction

Martensitic Transformation (MT) is a widely observed metallurgical phenomenon in different metals and alloys, which produces complex microstructure with multivariant product α variants [1- 5]. Materials with martensitic microstructure are of significant importance for a wide variety of engineering and industrial applications. Many research works have been reported with the purpose of explaining the crystallographic features through different simplified phenomenological models [6- 8].

However, the phenomenological models are not able to simulate the microstructure evolution under different conditions, which is important to control texture and microstructure and subsequently the final mechanical properties of the material. Since the micro-elasticity theory was proposed by Khachaturyan and Shatalov [9- 10] (KS theory), Phase Field Modelling (PFM) has been extensively employed to study the microstructure evolution, crack propagation, dislocation dynamics and other related phenomena with combination of KS theory [11-13]. Wang built a comprehensive 3D PFM to capture the main crystallographic features by considering the internal transformation strain during MT [14]. Later on, a PFM coupled with chemical element potential was extended to polycrystalline systems by Jin [15] and Shi [16] with the virtual work theory. The dislocation dissociation and effect of defects on microstructure were also investigated through PFM simulation [17- 19]. Because most materials in engineering and industrial applications are

of a polycrystalline nature, it is important to predict the martensitic microstructure in polycrystals for material design and texture control purposes for different engineering application conditions. In the elastically inhomogeneous polycrystalline system, besides the interaction between grain boundaries and solute atoms, the presence of an internal stress field because of interacting crystallographic martensitic variants from different parent grains plays an essential role in microstructure evolution. In order to calculate the mechanical strain and stress fields within a heterogeneous polycrystalline assembly, two different PFM methods were proposed: (i) equivalent eigenstrain simulation system by Wang et al. [20] and (ii) efficient iterative-perturbation technique with Fourier spectral method by Hu and Chen et al. [21- 23]. Recently, the Hu- Chen iteration schedule was employed to study the hydride microstructure formation and interaction between deformation twins and grain boundaries in polycrystals [24- 25]. Those calculation methods largely extend the application potential of PFM in material science and engineering.

Compared with a single crystalline material, the complication of simulating a polycrystalline assembly is caused not only by the elastic heterogeneity, but also by the strain relaxation at grain boundaries and the plastic deformation accumulated by growth of martensite plates. Guo et al. [26] introduced the plastic deformation for microstructure evolution in an elastoplastic phase field model. This model allows the elastic strain during MT to be relaxed partly by plastic deformation with an extra TDGL (Time-Dependent Ginzburg Landau) equation once the local stress exceeds the assumed yield stress [27- 29]. It has been shown that the plastic deformation can change the morphology of variant plates somehow and favor the procedure of martensitic transformation in different boundary conditions [30]. In a more complicated approach, the strain hardening was taken into consideration to investigate the effect of grain size on martensite formation in steels within a linear isotropic relationship by Yeddu [31]. Another relaxation mechanism for transformation strain is related to the grain boundaries. The phenomenon of grain-boundary relaxation on plasticity of nanocrystalline Fe has been observed [32]. By assuming that GBs have an open internal structure, ignoring the interaction of dislocations within grain boundaries, the product martensitic variants should nucleate at grain boundaries due to the grain-boundary relaxation on misfit strain. Heo et al. [33] proposed a misfit strain relaxation parameter and studied the effect of this parameter and curvature of grain boundary on the nucleation mechanism around grain boundaries in polycrystals. Besides the effect of internal factors within polycrystals, it has been proven that the interaction between external loading and internal elastic strain can favor or suppress the growth of selected variants during MT within a single crystal [34- 35].

In this study, the microstructure evolution is investigated with different conditions in polycrystalline parent grains. For simplicity, two alpha variants of Ti-6Al-4V alloy are under consideration in 2D dimensions. Simulation of nucleation and growth of variants with and without applied stress, plastic deformation and strain hardening are conducted. Finally, the microstructure evolution with the condition of mixing all internal and external factors that can change the stress and strain fields are captured in 2D and 3D dimensions is the main objective in the present paper; i.e. to simulate the microstructure evolution under relatively realistic condition.

2. Phase-field modelling

For polycrystals, under isothermal conditions and ignoring the solute-grain boundary interaction effect, the microstructure evolution is governed mainly by the Gibbs free energy G, which is composed of four components: the chemical free energy G^{chem}, the gradient energy G^{grad}, the elastic strain energy G^{el} and the mechanical energy through external loading G^{appl}:

$$G = \int (G^{chem} + G^{grad} + G^{el} + G^{appl}) dv \quad (1)$$

Similar to the Gibbs energy formula, different energy can be constructed with the non-conversed structural parameters $\eta_{pg}(\boldsymbol{r}, t)$ that are located between 0 and 1, where

$\eta_{pg}(\boldsymbol{r},t)$= 1 means that the point $\boldsymbol{r}$ is located in the pth martensitic variant from the gth parent grain, while $\eta_{pg}(\boldsymbol{r},t)$= 0 means the point $\boldsymbol{r}$ is out of pth variant from the gth parent grain. The different types of energies considered in this phase field model will be explained in the following sections.

2.1. Chemical free energy

By setting the temperature and pressure as constants, the local chemical free energy without solute drag effect around the grain boundary is given as [30, 33]:

$$G^{chem} = \frac{1}{V_m}[\frac{A}{2}\sum_g\sum_p \eta_{pg}^2(\mathbf{r},t) - \frac{B}{3}\sum_g\sum_p \eta_{pg}^3(\mathbf{r},t) + \frac{C}{4}(\sum_g\sum_p \eta_{pg}^2(\mathbf{r},t))^2] \quad (2)$$

Based on Yeddu [30], the Landau coefficients A, B and C are related to the driving force ΔG_m and the Gibbs activation energy barrier ΔG^* that prevents the martensitic transformation to proceed by A= $32\Delta G^*$, B= 3A+ $12\Delta G_m$ and C= 2A+ $12\Delta G_m$, while the driving force is the difference of Gibbs free energy between β and α phase in equilibrium state, V_m is the molar volume.

2.2. Gradient energy

In polycrystals, the gradient energy under a non-equilibrium condition at the grain boundaries is expressed as:

$$G^{grad} = \frac{1}{2}\sum_g\sum_p k_{ij,pg}|\frac{\partial\eta_{pg}(r,t)}{\partial x_i}||\frac{\partial\eta_{pg}(r,t)}{\partial x_j}| \quad (3)$$

Where $k_{ij,pg}$ is the gradient energy coefficient in the form of a symmetric tensor that characterizes the gradient energy within boundaries of different variants. From Shi's work [34], due to the dislocations and structural ledge in different facets of variants, the interfacial energies depend on the misorientation between variants. In polycrystals with different crystallographic orientations of parent β grains, the anisotropic interfacial energy function of the parent structure is not known in detail. Therefore, in the current work we assume that the interfacial energy of the parent structure is isotropic. As a result, the $k_{ij,pg}$ is set to be a constant k related to the interfacial energy γ by the following equations [30]:

$$\Delta G^* = \frac{3\gamma V_m}{4\sqrt{2}\delta},\ k = \frac{3\gamma\delta}{2\sqrt{2}} \quad (4)$$

Where δ is the interface thickness.

2.3. Elastic energy

In the MT, the elastic strain energy triggered by misfit strain between parent grains and product variants is one of the main contributions to the thermodynamics and kinetics of martensitic transformation. In a polycrystalline system, the eigen strain of different variants is dependent on the orientation of parent grains as:

$$\varepsilon_{ij}^{00}(p,g) = a_{ik}^g\varepsilon_{kl}^{000}(p)a_{jl}^g \quad (5)$$

$$\boldsymbol{a}^g = \begin{bmatrix} cos\ \alpha_g & sin\ \alpha_g \\ -sin\ \alpha_g & cos\ \alpha_g \end{bmatrix} \quad (6)$$

Where $\varepsilon_{kl}^{000}(p)$ is the eigen strain of the p^{th} variant from the reference parent grain, $\boldsymbol{a}^g$ is the rotation of the g^{th} parent grain with respect to the reference parent grain in 2D, and the rotation in 3D is a 3×3 matrix [33]. Hereafter, the Einstein summation notation is applied for all tensorial relations. In the current work, the reference coordinate is set the same as in Shi's work [34]. Accordingly, with the assumption that the elastic tensor of the α phase is the same and isotropic as the one of the β phase, the elastic stiffness is a position-dependent modulus, which can be calculated as:

$$C_{pqrs}(\boldsymbol{r}) = \sum_g \phi_g(\boldsymbol{r})C_{ijkl}^{0000} \quad (7)$$

Where $\phi_g(\boldsymbol{r})$ is the structural parameter of the g^{th} parent β grain, and C_{ijkl}^{0000} is the elastic tensor in the reference coordinate system. Eq. (7) results in a smooth transition of the elastic tensor across grain boundaries between parent grains. The local eigen strain in poly-crystals is position-dependent with a linear relationship, as:

$$\varepsilon_{ij}^{0}(\boldsymbol{r}) = \sum_g \sum_p \eta_{pg}(\boldsymbol{r},t)\, \varepsilon_{ij}^{00}(p,g) \tag{8}$$

When the MT is progressing, the nucleation and growth of new variants lead to local deformation with small displacement $u_i(\boldsymbol{r})$, thus inducing the local actual strain $\varepsilon_{ij}(\boldsymbol{r})$. By following Khachaturyan and Shatalov's scheme [9- 10], the $\varepsilon_{ij}(\boldsymbol{r})$ can be separated in a homogeneous strain $\bar{\varepsilon}_{ij}$ and a heterogeneous strain $\delta\varepsilon_{ij}(\boldsymbol{r})$. Based on the small-strain approximation, the $\bar{\varepsilon}_{ij}$ and $\delta\varepsilon_{ij}(\boldsymbol{r})$ are expressed as :

$$\varepsilon_{ij}(\mathbf{r}) = \bar{\varepsilon}_{ij} + \delta\varepsilon_{ij}(\mathbf{r}) \tag{9a}$$

$$\bar{\varepsilon}_{ij} = \frac{1}{V_m}\int \varepsilon_{ij}(\boldsymbol{r})dv \tag{9b}$$

$$\delta\varepsilon_{ij}(\boldsymbol{r}) = \frac{1}{2}\left(\frac{\partial u_i(\boldsymbol{r})}{\partial r_j} + \frac{\partial u_j(\boldsymbol{r})}{\partial r_i}\right) \tag{9c}$$

The local elastic strain $\varepsilon_{ij}^{el}(\boldsymbol{r})$ is the difference between the local actual strain and the local eigen strain, given by:

$$\varepsilon_{ij}^{el}(\boldsymbol{r}) = \varepsilon_{ij}(\boldsymbol{r}) - \varepsilon_{ij}^{0}(\boldsymbol{r}) \tag{10}$$

Since the mechanical equilibrium is established fast and assumed to be reached instantly, the following equation for mechanical equilibrium is employed [29]:

$$\sigma_{ij}(\boldsymbol{r}) = C_{ijkl}(\boldsymbol{r})\varepsilon_{kl}^{el}(\boldsymbol{r}) \tag{11a}$$

$$\frac{\partial \sigma_{ij}(\boldsymbol{r})}{\partial r_j} = 0 \tag{11b}$$

Different from the elastically homogeneous single crystal, the heterogeneous strain fields are different among different parent β grains. In order to compute the elastic strain in a polycrystal, the Hu-Chen scheme [21- 23] is employed here. The position-dependent elastic tensor $C_{pqrs}(\boldsymbol{r})$ is divided in two parts: the constant homogeneous part C_{pqrs}^{refer} and the heterogeneous part $C_{pqrs}^{heter}(\boldsymbol{r})$ related to the position:

$$C_{pqrs}(\boldsymbol{r}) = C_{pqrs}^{refer} + C_{pqrs}^{heter}(\boldsymbol{r}) = C_{pqrs}^{refer} + \left(\sum_g \phi_g(\boldsymbol{r}) a_{ip}^{g} a_{jq}^{g} a_{kr}^{g} a_{ls}^{g} C_{ijkl}^{0000} - C_{pqrs}^{refer}\right) \tag{12}$$

Where the C_{ijkl}^{refer} is the average of maximum and minimum of $C_{pqrs}(\boldsymbol{r})$. In this study the elastic displacement $u_i(\boldsymbol{r})$ is computed iteratively until the convergence ν of displacement is smaller than the pre-set tolerance 10^{-4} in 2D:

$$\nu = \sqrt{\int [(u_1^{n+1} - u_1^{n})^2 + (u_2^{n+1} - u_2^{n})^2]dv} \tag{13}$$

Finally, the elastic strain energy G^{el} is given as:

$$G^{el} = C_{ijkl}(\boldsymbol{r})\varepsilon_{ij}^{el}(\boldsymbol{r})\varepsilon_{kl}^{el}(\boldsymbol{r}) \tag{14}$$

2.4. External loading energy

Under the external loading σ_{ij}^{appl}, the mechanical strain energy due to interaction between applied stress and elastic strain ε_{kl}^{el} is:

$$G^{appl} = -\sigma_{ij}^{appl}\varepsilon_{ij}^{el}(\boldsymbol{r}) \tag{15}$$

2.5. Kinetic function

Because no long-range diffusion occurs during MT, only the Allen-Cahn equation, also known as time-dependent Ginzburg-Landau (TDGL) equation, is employed in the present work to capture the microstructure evolution:

$$\frac{\partial \eta_{pg}}{\partial t} = \phi_g(\boldsymbol{r})[-L\frac{\delta G}{\delta \eta_{pg}} + \xi_{pg}(\boldsymbol{r},t)] \quad (16)$$

Where L is the kinetic coefficient and $\xi_{pg}(\boldsymbol{r},t)$ is the Langevin random noise term that describes the local thermal fluctuation of the structural order parameters [36-38]. In Ref. [36-38], the details of Langevin random noise are explained. Different to the TDGL equation for a single crystal, the extra factor $\phi_g(\boldsymbol{r})$ in Eq (16) represents the structural parameter of parent grains, which can guarantee that only the variant η_{pg} is evaluated within the g^{th} parent grain.

2.6. Nucleation model at grain boundaries

Theoretically, defects such as grain boundaries may act as prior nucleation sites as observed by Olson et al. [39- 40]. In order to simulate the event of nucleation at grain boundaries, the nucleation model proposed by Heo [33] is implemented here. In terms of grain boundary relaxation on transformation strain, Eq. (5) is modified with a interpolation function $\psi(\boldsymbol{r})$, as:

$$\varepsilon_{ij}^{00}(p,g,\boldsymbol{r}) = \psi(\boldsymbol{r})a_{ik}^{g}a_{jl}^{g}\varepsilon_{kl}^{000}(p) \quad (17)$$

The interpolation function $\psi(\boldsymbol{r})$ is related to the structural parameters $\phi_g(\boldsymbol{r})$ of parent grains and a grain boundary relaxation parameter ρ, in the following manner:

$$\psi(\boldsymbol{r}) = \frac{\rho(\varphi_{max}-\varphi(\boldsymbol{r}))+(\varphi(\boldsymbol{r})-\varphi_{max})}{\varphi_{max}-\varphi_{min}} \quad (18)$$

$$\varphi(\boldsymbol{r}) = \sum_g \phi_g^2(\boldsymbol{r}) \quad (19)$$

Where φ_{max} and φ_{min} are the maximum and minimum value of $\varphi(\boldsymbol{r})$. In this study, the effect of the grain boundary relaxation parameter ρ and the curvature of grain boundary are not taken into consideration. Therefore, ρ is set as a constant, and the parent grains map is obtained by the simple Allen-Cahn equation.

2.7. Plasticity and strain hardening model

Normally, due to the thermal activation of dislocation movement by increasing temperature, the yield stress of most materials keeps decreasing and plastic deformation occurs easily. In Ti-6Al-4V alloy, the temperature of the martensitic transformation is above 900 K and the yield stress is ~ 500MPa [42- 44]. Hence, plastic relaxation following elastic strain should be considered. Additionally, the phenomenon of strain hardening will take place with plastic strain accumulation during growth of the martensitic plates. The plasticity and strain hardening model will be explained in detail below.

With MT progressing, the local equivalent stress may exceed the yield stress, subsequently local plastic deformation occurs and a part of the local actual stress is relaxed. Although Ti-6Al-4V is a highly anisotropic alloy, the yield stress surface is assumed to be isotropic for simplicity. Assuming that the Ti-6Al-4V alloy is perfectly elastic- plastic without strain hardening, the yield stress is considered to be constant. The Von Mises yield criterion is considered here [29- 31]:

$$\sigma_{eq}^2 - \sigma_y^2 = \sigma_{11}^2 - \sigma_{11}\sigma_{22} + \sigma_{22}^2 + 3\sigma_{12}^2 - \sigma_y^2 > 0 \quad (20)$$

Once the Von Mises equivalent stress is larger than the yield stress, local plasticity is initiated. The evolution of local plastic strain is related to the elastic shear strain energy density G^{shear} and governed by another TDGL equation [26]:

$$\frac{\partial \varepsilon_{ij}^{pl}(\boldsymbol{r})}{\partial t} = -K_{ijkl}\frac{\partial G^{shear}}{\partial \varepsilon_{kl}^{pl}(\boldsymbol{r})} \quad (21)$$

Where $K_{ijkl} = (kc_{ijkl})^{-1}$ is the plastic kinetic coefficient that controls the local plastic strain relaxation effect, c_{ijkl} is the local elastic tensor in Eq. (7), and k is a constant for

simplicity. The elastic shear strain energy density G^{shear} is a function of local elastic shear strain as:

$$G^{shear} = \frac{1}{2}\int c_{ijkl}(e_{ij}(\boldsymbol{r})- e^0_{ij}(\boldsymbol{r}))(e_{ij}(\boldsymbol{r})- e^0_{ij}(\boldsymbol{r}))dv \quad (22)$$

Where $e_{ij}(\boldsymbol{r})$ and $e^0_{ij}(\boldsymbol{r})$ are the deviatoric strain components of local actual strain and local eigen strain. It should be pointed out that with consideration of plastic deformation, the local actual strain is partly relaxed by plastic strain. Therefore, the local actual strain (Eq. (9a)) should be modified as:

$$\varepsilon_{ij}(\boldsymbol{r}) = \bar{\varepsilon}_{ij} + \delta\varepsilon_{ij}(\boldsymbol{r}) + \varepsilon^{pl}_{ij}(\boldsymbol{r}) \quad (23)$$

And the deviatoric strains of local actual strain and eigen strain in 2D are:

$$e_{ij}(\boldsymbol{r}) = \varepsilon_{ij}(\boldsymbol{r}) - \frac{1}{2}\varepsilon_{ij}(\boldsymbol{r})\delta_{ij} \quad (24a)$$

$$e^0_{ij}(\boldsymbol{r}) = \varepsilon^0_{ij}(\boldsymbol{r}) - \frac{1}{2}\varepsilon^0_{ij}(\boldsymbol{r})\delta_{ij} \quad (24b)$$

Where δ_{ij} is Kronecker delta function.

When strain hardening is considered, the yield stress changes as a function of microstructure evolution and is expressed as summation of yield stress from revised Hall-Petch effect σ^0_y and strain hardening σ^n_y:

$$\sigma_y(\boldsymbol{r}) = \sigma^0_y(\boldsymbol{r}) + \sigma^n_y(\boldsymbol{r}) \quad (25)$$

The yield stress $\sigma^0_y(\boldsymbol{r})$ obtained from the revised Hall-Petch effect is related to the volume fraction of local α variants based on the report by Galindo-Fernández [45]. The $\sigma^n_y(\boldsymbol{r})$ is obtained through the Johnson-Cook hardening law [46], as:

$$\sigma^0_y(\mathbf{r}) = [\sigma_\alpha \sum_g \sum_p \eta^2_{pg}(\boldsymbol{r}) + \sigma_\beta\left(1 - \sum_g \sum_p \eta^2_{pg}(\boldsymbol{r})\right) + \frac{k_{HP}}{\sqrt{D_\alpha}}]F(T, \dot{\varepsilon}) \quad (26a)$$

$$F(T, \dot{\varepsilon}) = \left(\frac{\varpi\mu b^3}{k_B T \ln(10^7/\dot{\varepsilon})}\right)^{n_{HP}} \quad (26b)$$

$$\sigma^n_y(\boldsymbol{r}) = \left[a + b\left(1 + m_1 ln\frac{T}{T_r}\right)(\varepsilon_{pl}(\boldsymbol{r}))^n\right]\left(1 + cln\frac{\dot{\varepsilon}}{\dot{\varepsilon}_{ref}}\right)[1 - (\frac{T-T_r}{T_m-T_r})^{m_2}] \quad (26c)$$

With Eq. (26), the local yield stress is related to the local variant volume $\eta_{pg}(\boldsymbol{r})$ which is the volume of the p^{th} martensite product variant originating from crystal orientation g of the parent structure with local plastic equivalent strain $\varepsilon_{pl}(\boldsymbol{r})$. Here, the strain rate $\dot{\varepsilon}$ is assumed to be 1 and have no effect on the local yield stress. The physical meaning of other parameters can be found in Ref. [45- 47].

3. Simulation parameters and models

In the current study the following simulation parameters are used:

(1) the simulation system consists of 1024* 1024 grid points with a mesh size of 25 nm in 2D dimensions. 16 parent β grains are prepared through the TDGL function, and the structural parameters of parent grains sum up to 1: $\sum_{g=1}^{16}\phi_g(\boldsymbol{r}) = 1$. For simplicity, only two α variants can be transformed from a single parent β grain, i.e. p = 1, 2 in the above equations. Based on Shi's work [34], the considered 2 variants are selected by setting the orientation of parent grain as (0 0 0) and ignore the small component along z axis being 0.0003. Therefore, all the SFTS and elastic tensors need to be rotated based on the crystallographic orientation of corresponding parent β grains;

(2) the driving force ΔG_m is obtained based on Lindwall's work [43] by setting temperature at 1073 K and the equilibrium compositions of α and β phases as Ti-10.25Al-3.21V and Ti-9.01Al-10.99V (at%), respectively.

(3) the thickness of the interfacial region is 5 grid points and the interfacial energy is 50 mJ/m^2. The kinetic coefficient L and time step dt are $1.6 * 10^{-7}$J/m^3/s and $2 * 10^{-3}s$, respectively. The molar volume V_m is assumed to be 10^{-5}m^3/mol [34]. All the simulations are conducted with clamped boundary conditions.

(4) the elastic tensor of the α phase is assumed to be the same and isotropic as the one of the β phase, which is taken as: c_{11} = 97.7GPa, c_{12} = 82.7GPa and c_{44} = 37.5GPa in Voigt notation. The eigen strain of 2 variants in reference state is given as :

$$\varepsilon_{ij}^{000}(1) = \begin{bmatrix} \varepsilon_{11}^{000} & 0 \\ 0 & \varepsilon_{22}^{000} \end{bmatrix}, \qquad \varepsilon_{ij}^{000}(2) = \begin{bmatrix} \varepsilon_{22}^{000} & 0 \\ 0 & \varepsilon_{11}^{000} \end{bmatrix} \tag{27}$$

Where ε_{11}^{000}= -0.049 and ε_{22}^{000}= 0.067, taken from Ref.[34]. The orientations of 16 parent β grains are taken randomly.

(5) with regard to the external loading, the applied tensile and compressive stress is 50MPa along Y direction, which has obvious effect on the microstructure. More details about the applied stress can be found in the Ref. [34- 35]. The yield stress is set as 880MPa without considering strain hardening at room temperature [49]. And the simulation parameters for strain hardening described by Eq. (25) and (26) can be found in Ref. [45- 46].

(6) for the nucleation event, Langevin random noise is added in the early simulation stage, while for growth event under different conditions, a small seed with 2×2 grids is put in the center of the simulation map without random noise in Eq. (16).

(7) in terms of microstructure evolution in 3D dimensions, the simulation model is conducted with nucleation and growth under conditions of external compression loading and plastic deformation with strain hardening. The functions that relate mechanical stress and strain fields are needed to extend into 3D dimensions. The structural map consist of 8 parent β grains with random crystallographic orientations transforming to 4 different α variants with following eigen strain in reference state:

$$\varepsilon_{ij}^{000}(1) = \begin{bmatrix} -0.0490 & -0.0031 & 0 \\ -0.0031 & 0.0670 & 0 \\ 0 & 0 & -0.0003 \end{bmatrix}, \quad \varepsilon_{ij}^{000}(2) = \begin{bmatrix} -0.0490 & 0 & -0.0031 \\ 0 & -0.0003 & 0 \\ -0.0031 & 0 & 0.0670 \end{bmatrix},$$

$$\varepsilon_{ij}^{000}(3) = \begin{bmatrix} 0.0334 & -0.0222 & -0.0253 \\ -0.0222 & -0.0100 & 0.0412 \\ -0.0253 & 0.0412 & -0.0056 \end{bmatrix}, \quad \varepsilon_{ij}^{000}(4) = \begin{bmatrix} 0.0334 & -0.0253 & -0.0222 \\ -0.0253 & -0.0056 & 0.0412 \\ -0.0222 & 0.0412 & -0.0100 \end{bmatrix},$$

(8) based on Heo and Yamanaka's work [28, 33], the grain boundary relaxation parameter ρ is taken as 0.29 (Eq. (18)), the plastic kinetic coefficient k is take as 0.001 (Eq. (21)).

(9) the morphology of the transformed α variant is outlined based on the condition : $\eta_{pg}^2(\boldsymbol{r}) > 0.5$.

(10) for convenient calculation, the TDGL equation is implemented in a reduced scale. All calculated parameters are dimensionless based on Ref. [50]. The energy scaling factor and normalization factors are set as $\Delta\tilde{G}$= $|\Delta G_m|$(driving force), $\Delta M = 10^{-1}$ m^2 mol/J/s.

(11) all recorded videos of the simulations with different conditions are shown in the supplementary materials section.

With simulation parameters above, several simulations are performed in different conditions below:

Table 1 Phase field simulation cases with different conditions

	Nucleation	Growth
Case 1	A	A
Case 2	B	B
Case 3	C	C
Case 4	-	B+C
Case 5	-	B+D+E

A: No applied stress; B: Tension along Y axis; C: compression along Y axis;
D: Plastic deformation; E: Strain hardening

4. Results and discussion

4.1. Parent β grains map preparation

To simulate the martensitic transformation from the β phase to the α phase in a polycrystal, the structural map with 16 β grains is prepared firstly by a simple TDGL equation below:

$$F = \int \left(\frac{1}{4} - \frac{1}{2}\sum_{g=1}^{16}\phi_g^2 + \frac{1}{4}\sum_{g=1}^{16}\phi_g^4 + \frac{3}{4}\sum_{p=1}^{16}\sum_{\substack{q=1 \\ q\neq p}}^{16}\phi_p^2\phi_q^2 + \frac{1}{2} * 2 * \sum_{g=1}^{16}\left|\nabla\phi_g\right|^2\right)dv \quad (28a)$$

$$\frac{\partial\phi_g}{\partial t} = -L_g\frac{\delta F}{\delta\phi_g} \quad (28b)$$

16 randomly distributed seeds are set as the initial microstructure, and enough evolution time is guaranteed to make sure that the prepared initial microstructure is occupied only by β phase. The simulated initial β microstructure is shown as Figure 1 below, and then random orientations are assigned to each parent β grain.

In the parent beta grain structure below, some of the triple junctions do not hold 120º. It is surmised that there are two reasons for the triple junctions to deviate from the equilibrium value of 120º: 1) the parent structural map was simulated by Phase-field model in periodic condition; and 2) the parent map is shown in 2D, which is a cross-section of the 3D crystallographic structure. Therefore, some of the triple junctions appear to exhibit a deviatoric dihedral angle.

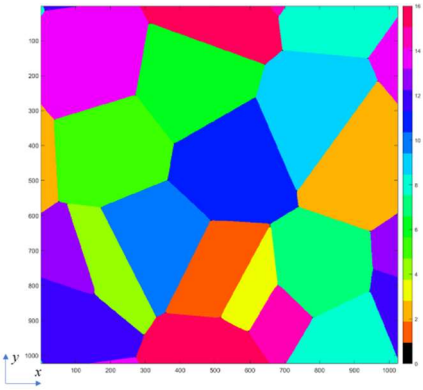

Figure 1. The initial polycrystalline structure of 16 parent β grains.

4.2. Nucleation without external loading

Figure 2 shows the microstructure evolution of α variants in the nucleation and early growth stage without applied stress. The parent β grains are set as background in cyan color (Figure 2 (b)~ (f)). It can be seen that with enough local structural fluctuation by random noises, small near-spherical variants have nucleated, as pointed out in Figure 2 (a), and then several positions served as nucleation sites (Figure 2 (c)). Later on, those variants grow into the parent β grains in the shape of needles by following different growth directions (Figure 2 (c)~ (f)). The orientations of variants from different parent grains depend on the orientation of the parent grains. Comparing Figure 2 (b)~ (d) with Figure 1, it is clear that due to the relaxation effect of misfit strain at grain boundaries, different nuclei appeared at grain boundaries, which is consistent with experimental observations [50- 52]. It is interesting to mention that only with grain boundary relaxation, some triple junctions act as prior sites for nucleation, as seen in Figure 2 (b) and (c), but some other triple grain boundaries and one special quadruplet position in Figure 1 are not nucleation site. This would be related to the misorientation between parent grains.

In order to illustrate the local stress distribution, the Von Mises equivalent stress is calculated and shown in Figure 3. It is obvious that during the MT process, the local stresses are concentrated around α variants. Within the interior of variants, the Von Mises equivalent stress reaches the minimum value, while the interaction of variants leads to

increase of local stress (Figure 3 (f)). It is consistent with the stress distribution from Qiu. et al. [53] that the distribution of local stress around a single variant is symmetrical, and the variants grow following the direction where the local stress is relatively small around the tips of α plates, as indicated in Figure 3 (f). it should be mentioned that even in the early simulation stage, the maximum local equivalent stress is larger than the pre-set yield stress (880MPa), the local plastic deformation for nucleation is not under consideration here.

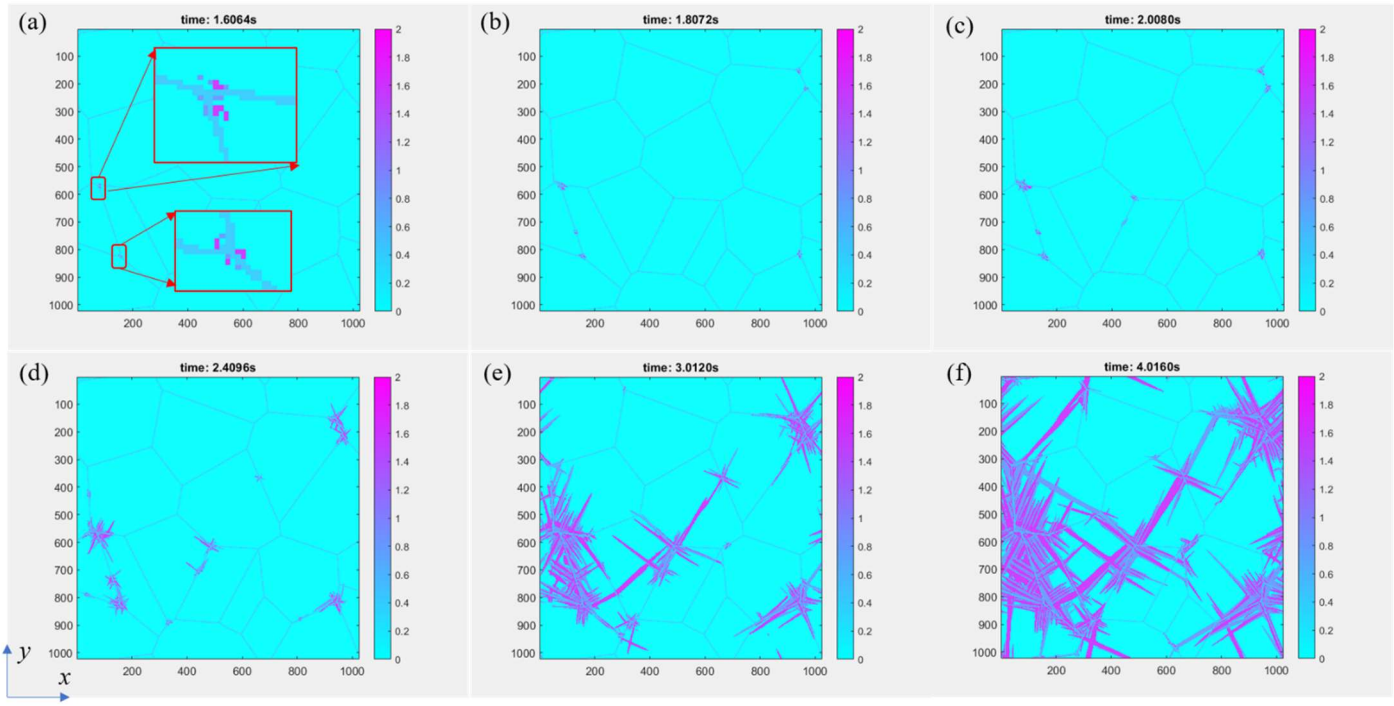

Figure 2. The nucleation and growth of α variants around grain boundaries with different simulation time.

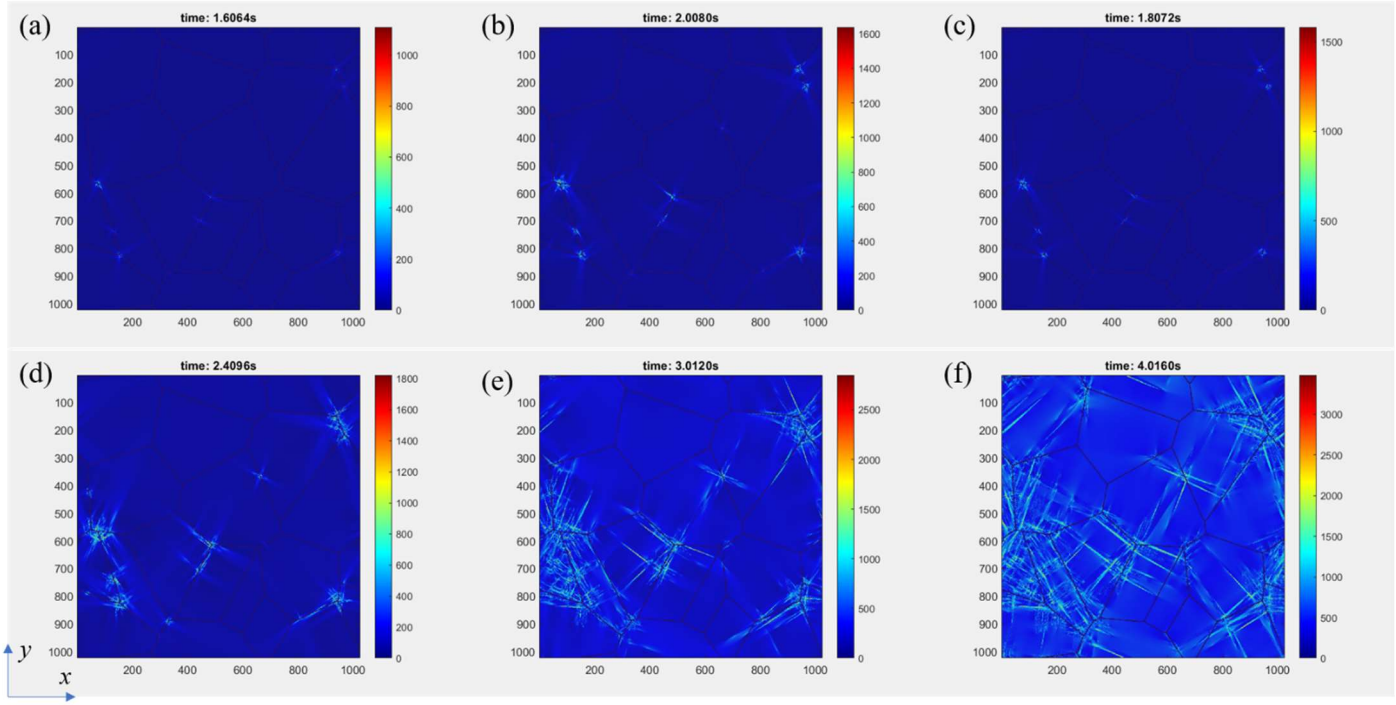

Figure 3. The distribution of Von Mises equivalent stress corresponding to microstructure in Figure 2.

4.3. Nucleation with external loading

As studied by Shi and Zhang [34- 35], the external tensile and compressive stresses have different effect on the microstructure evolution. Here the applied tensile and compressive stresses along the y direction are investigated to study the nucleation around grain boundaries and results are shown in Figure 4~ 7.

Under applied compressive stress, the variant nucleation occurs earlier than without applied stress, cf. Figure 4 (b), and the external loading favors the martensitic transformation by comparing the microstructure in Figure 4 with Figure 3. It is worth to note that some new variants nucleate at binary grain boundaries as demonstrated in Figure 4 (c)~ (e), which is different from the counterpart without loading. Figure ***5*** shows the distribution of local equivalent stress. From Figure ***5*** (a) it can be observed that the applied stress induced different stress fields within different parent grains. The local stresses are concentrated at binary and triple junction grain boundaries (Figure ***5*** (b) and (c)). By checking the Langevin noise, the amplitude of noise is small enough, thus its effect on the nucleation event can be ignored compared with the effect of external loading.

The nucleation of variants with applied tensile stress is different from the simulation with compressive stress, compared Figure ***6*** and Figure 7. Similar to conditions with compressive stress, the nucleation and growth of α variants are favored by external tensile stress, the occurrence of small α nuclei under tensile load is even earlier than the simulation results under compressive load. A striking difference between tensile and compressive conditions is that nucleation under tensile load is not always at grain boundaries, but within the interior of some parent grains, as seen in Figure ***6*** (b). Comparing the maps of stress fields in Figure ***5*** and Figure 7, it is found that the grain boundaries are the sites of stress concentration from the onset, which induced the formation of transformed α nuclei. With progressing MT in different parent grains, the local stresses are relaxed with different directions, which results in the growth of variants in different orientations.

Theoretically, the microstructure evolution during MT follows the path that reduces the Gibbs free energy of system. In the current study, the chemical free energy and interfacial energy are assumed to be isotropic, hence, the elastic strain energy density is considered to illustrate the distribution of energy in the system, as shown in Figure 8 with and without external loading. As illustrated by the red ellipses, within the interior of variants, the elastic strain energy reaches minimum values, while the interaction between different variants increase the local strain energy. The simulated nucleation occurring at triple junctions is consistent with the results from Xu [54].

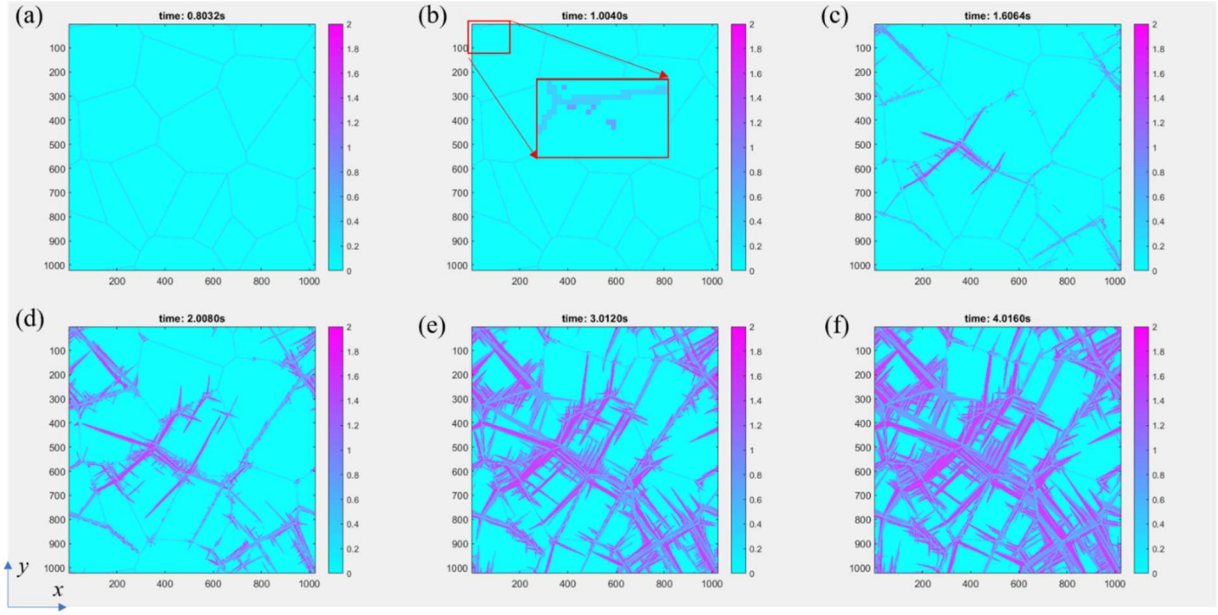

Figure 4. The nucleation and growth of α variants at grain boundaries with applied compressive stress for different simulation times.

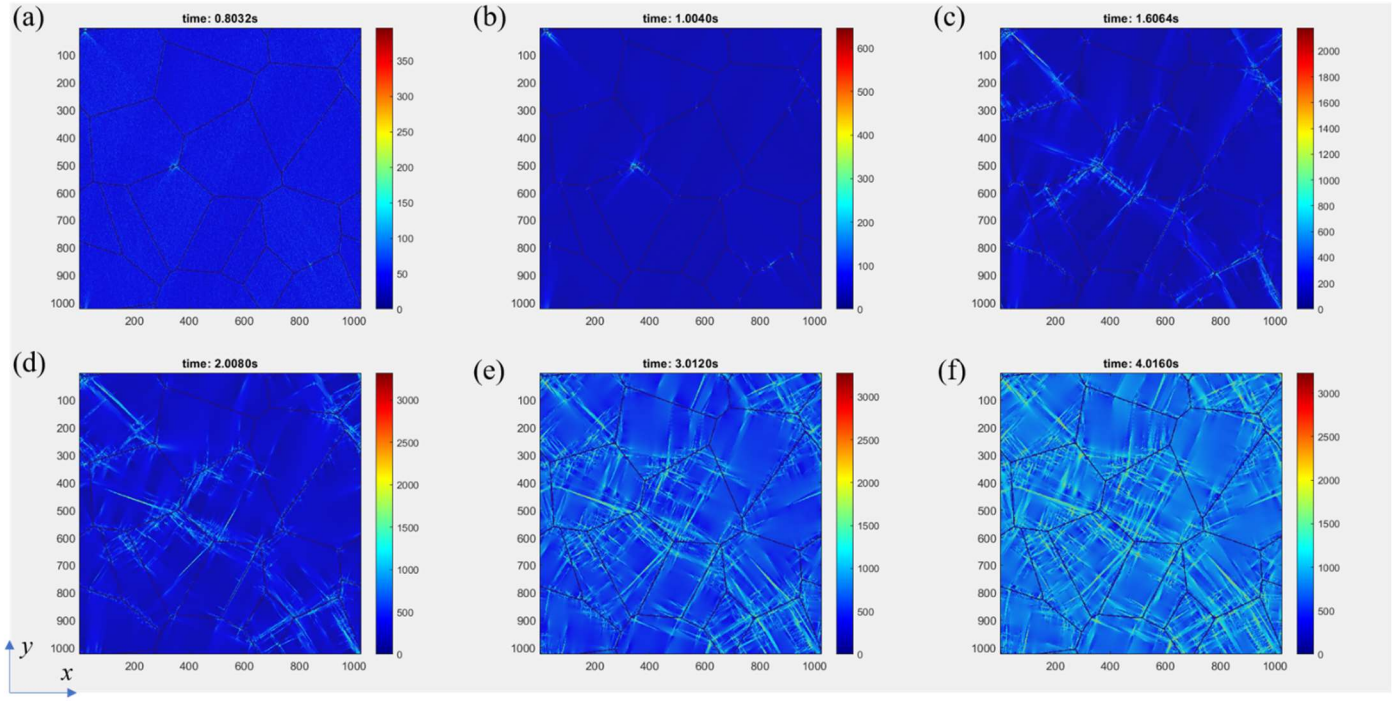

Figure 5. The distribution of Von Mises equivalent stress corresponding to microstructure in Figure 4.

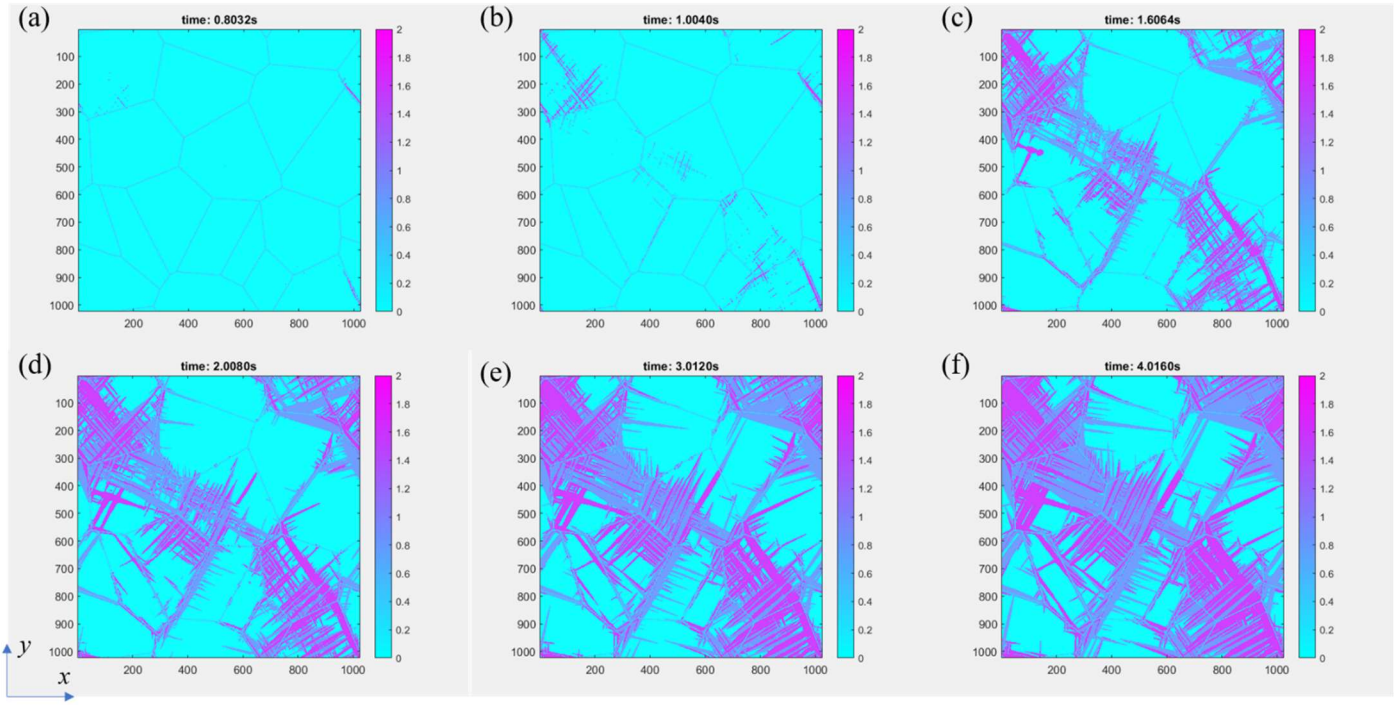

Figure 6. The nucleation and growth of α variants at grain boundaries under applied tensile stress for different simulation times.

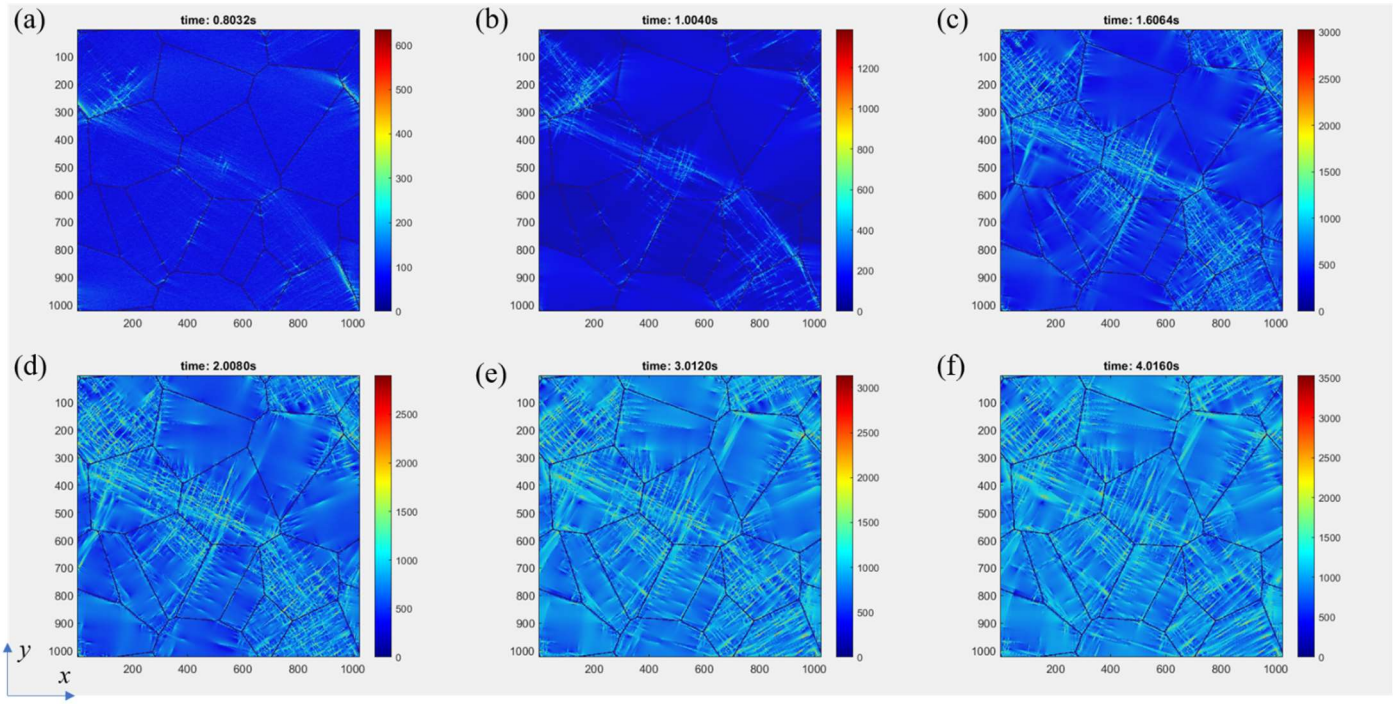

Figure 7. The distribution of Von Mises equivalent stress corresponding to the microstructures shown in Figure **6**.

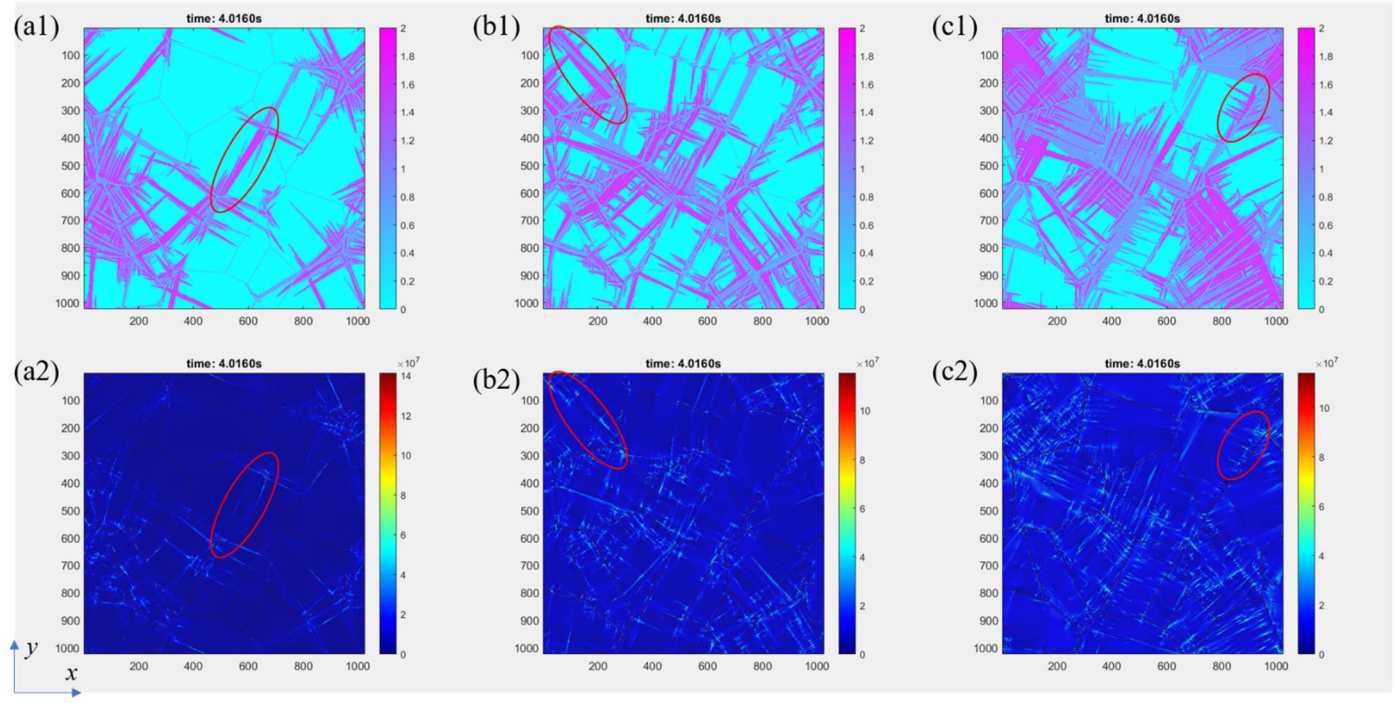

Figure 8. The distribution of variants and corresponding elastic strain energy with different conditions: microstructure at simulation time of 4.0106s in: a1: without external loading; b1: with compressive stress; c1: with tensile stress; elastic strain energy distribution at simulation time of 4.0106s in: a2: without external loading; b2: with compressive stress; c2: with tensile stress.

4.4. Variants growth without external loading

Figure 9 shows the growth of variants without plastic deformation or external loading. At the onset, due to the sharp interface between pre-set seed of α variants and β matrix, a part of the seed is relaxed into grain boundaries without $\eta_{pg}^2(\boldsymbol{r}) > 0.5$. Therefore, no variant is outlined, cf. Figure 9 (a). With growth of variants, a small rectangular shaped

variant appears in the center, cf. Figure 9 (b). Afterwards, the small variant grows into a cross-star shape, and enhances the occurrence of a second variant (Figure 9 (c)), which is known as an autocatalytic event, i.e. the new variant can be formed from the untransformed areas because of the high local elastic strain energy introduced by the previous existing variants [53]. When the variants keep growing into their parent grain and meet the β grain boundaries, as indicated in Figure 9 (d), new variants can be transformed from the matrix, but with different orientations from the first ones. With MT progress, more and more β phase matrix volume is transformed in needle shaped martensite grains. It should be mentioned that the small variants with cross-star shape gradually evolved in a martensite plate structure. The early variants with cross-star shapes reflect the symmetry of the misfit strain, but subsequently the interaction between variants break the symmetric distribution of the local elastic strain energy. As discussed above, the elastic strain energy within the interior of variants is smallest, which implies that the growth of variants can decrease the elastic strain energy of the system. Such a martensitic microstructure has been observed in our previous work (Figure 10) and by other researchers [55- 59]. In general, it could be said that there are various sources that may induce microstructural anisotropy: GB energy, mobility and (elastic) eigenstrain anisotropy. In the current work only the latter type of anisotropy was considered whereas other sources of anisotropy were ignored. It was proven that by only considering the elastic eigenstrain anisotropy, a needle-shaped martensitic structure can be simulated. Of course, these results do not exclude that other sources of anisotropy may have an effect as well. However, this was beyond the scope of the current work.

A line shown in Figure 9 (c) is selected to display the distribution of η_{pg}^2, elastic strain energy and Von Mises equivalent stress, cf. Figure 11. It is clear that for the 2 variants from the 11th parent β grain, the elastic strain energy is almost equal to the β matrix, while the elastic strain energy is relatively high at the interface, which supports the conclusion that the MT follows the path that reduces the Gibbs free energy of system.

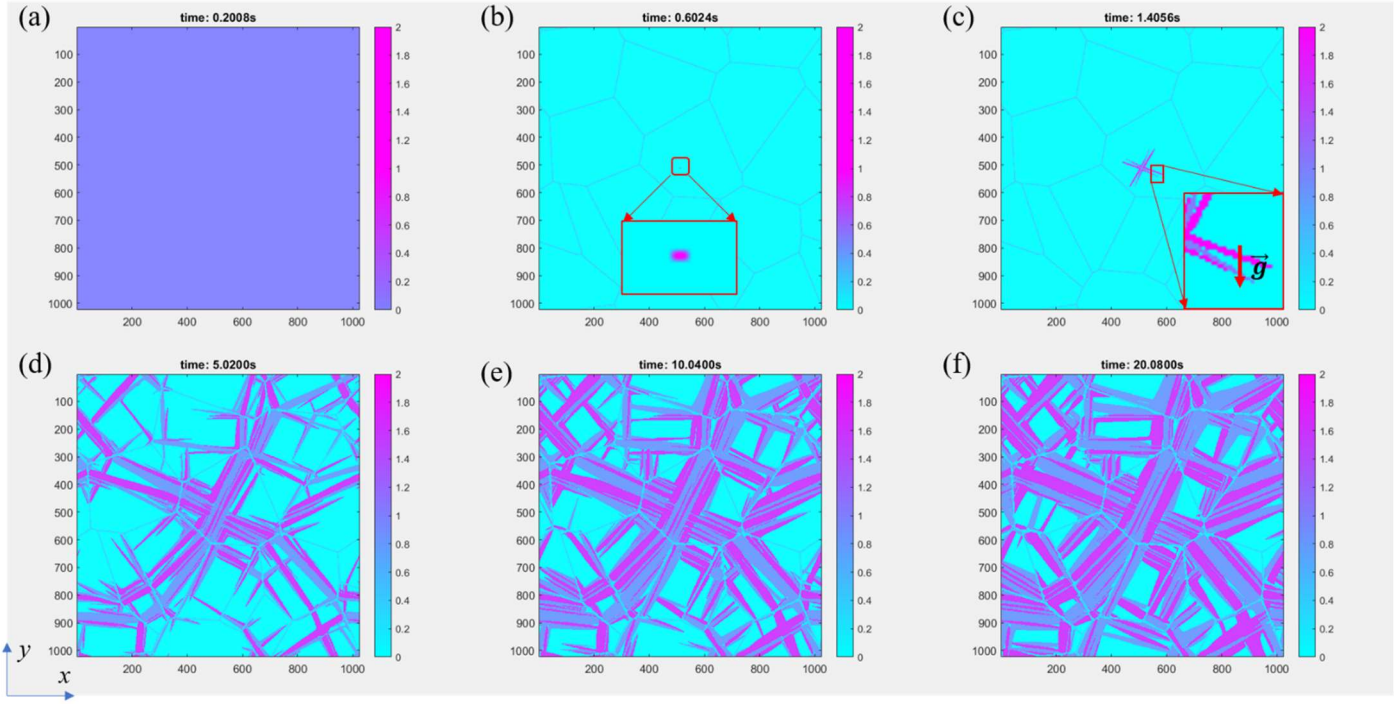

Figure 9. The growth of α variants from a pre-set seed without plastic deformation for different simulation times.

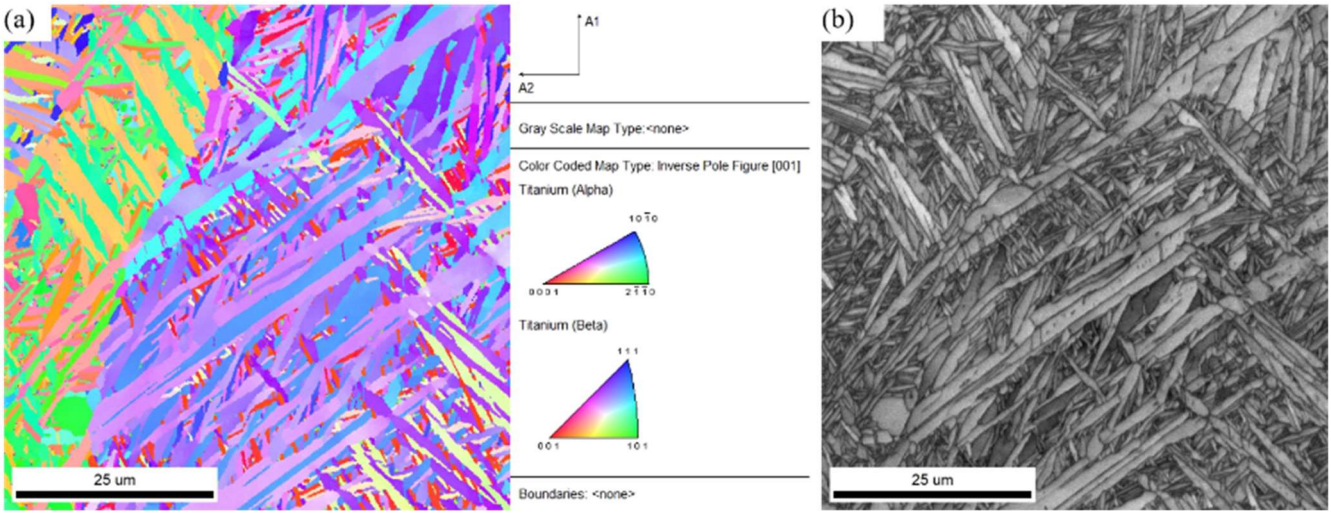

Figure 10. The observed martensitic microstructure with Selective Laser Melted Ti-6Al-4V.

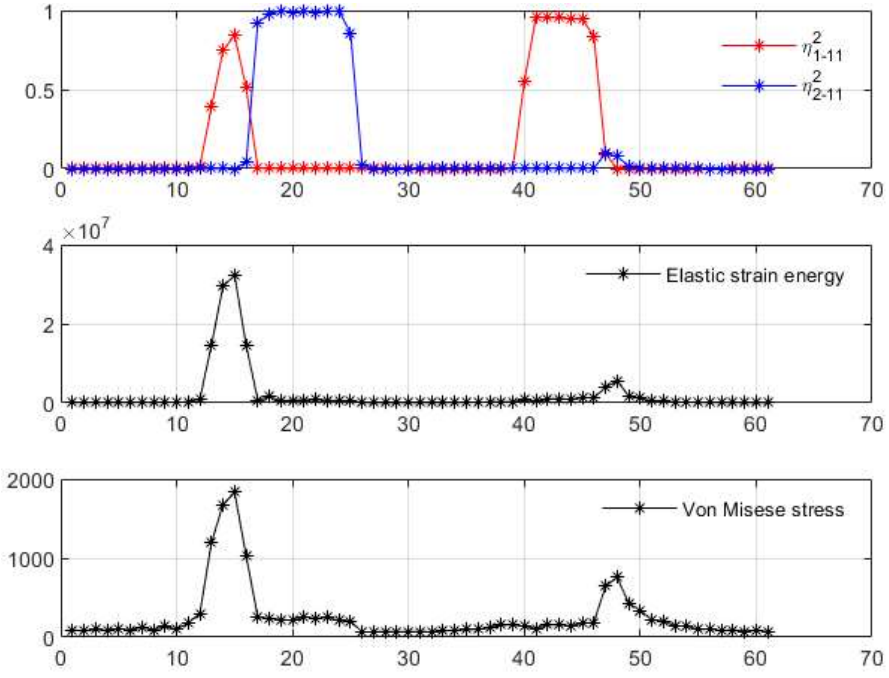

Figure 11. The distribution of of η^2_{pg}, elastic strain energy and Von Mises equivalent stress along the vector $\vec{g}$ in Figure 9.

4.4. Variants growth with external loading

Figure 12 displays the microstructure and distribution of elastic strain energy density under tensile and compressive load. Note that in order to study the effect of an external load on microstructure evolution with a multi-crystalline system, the misfit strain relaxation at grain boundaries is not taken into consideration here. It is clear that the applied stress has different effects on variant growth in the early stage of martensitic transformation for different parent β grains. By comparing Figure 12 with Figure 9, the difference of microstructure at the same simulation times implies that the external loading favors the MT kinetics, which can be explained by the interaction between applied stress and local elastic strain. Without applied stress, the nucleation and growth of new variants are driven by the accumulation of local elastic strain and stress. Even for the transformation in the adjacent parent grain, the new nucleus can occur only when the local elastic strain is beyond a critical value. But for the phase transformation under external load, the local elastic strain can work synergistically with the applied stress, which induces the

nucleation and growth of new variants in different parent β grains, while in some other β grains with different crystallographic orientation, nucleation and growth events are suppressed, as shown by the distribution of elastic strain energy. The induced variants by this interplay between applied stress and local strain are simulated and observed in Fe-0.3%C and other alloys [60- 61].

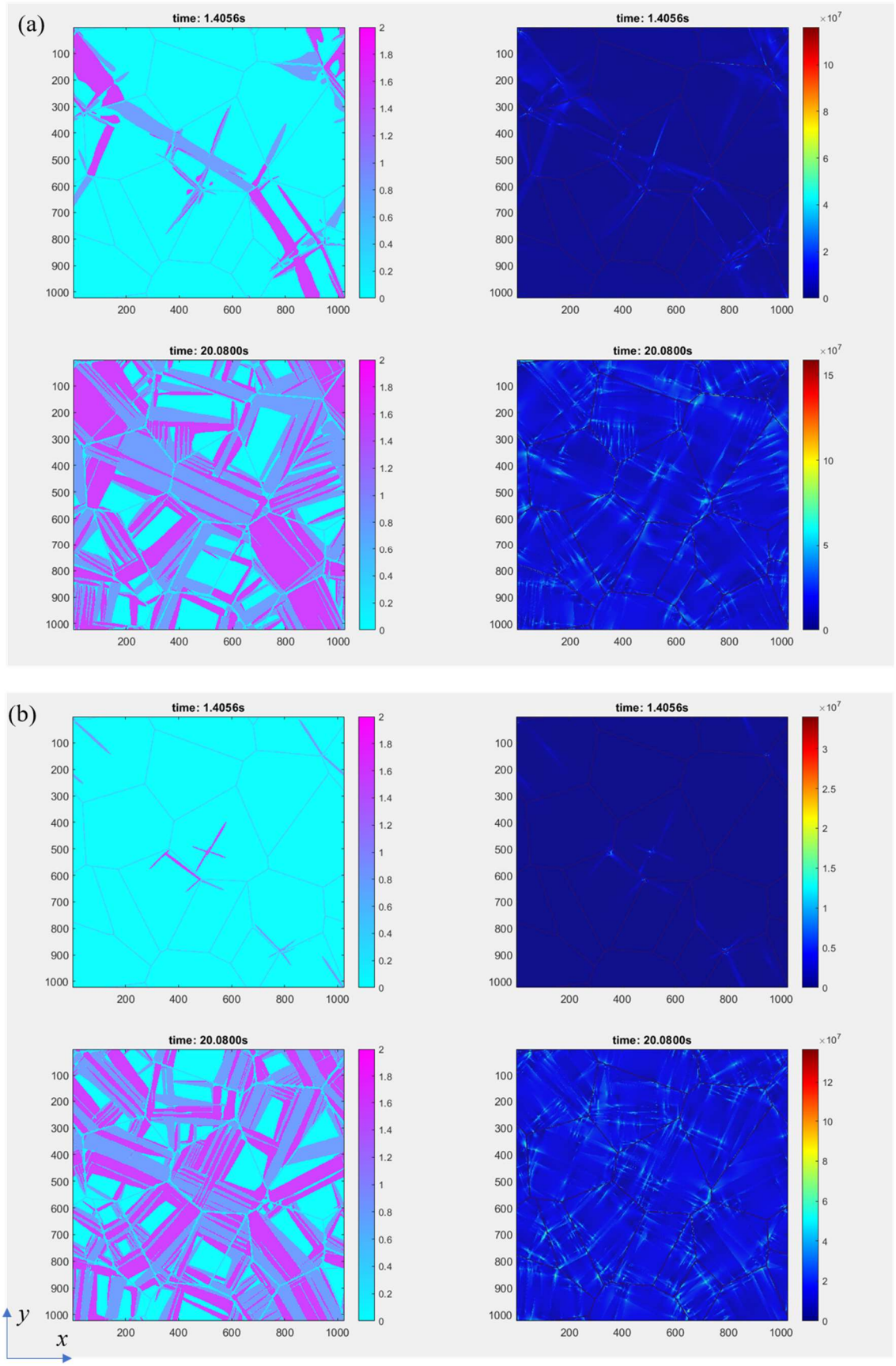

Figure 12. The microstructure and distribution of elastic strain energy with (a) tensile and (b) compressive stresses.

4.5. Variants growth with plastic deformation and strain hardening

Figure 13 and Figure 14 show the microstructure and equivalent plastic strain with simulation conditions of local plastic deformation, strain hardening and applied tensile load, respectively. With the local relaxation of elastic strain, the morphology of variants gradually change by assuming a coarse deviating from the initial plate shape, cf. ellipses in Figure 13 (d). Due to the small plastic kinetic coefficient in Eq. (21), the coarse growth of variants is not very obvious compared with simulation without plastic deformation, which implies that the plastic kinetic coefficient and plastic deformation should be considered during simulation of the MT. In the current work, the β matrix is assumed not to be plastically deformed, thus, no equivalent plastic strain is induced in the β matrix, which is different from earlier work by Yamanaka [28].

Figure 14 demonstrates the final microstructure with effect of plastic deformation combined with strain hardening and tensile stress. Compared with Figure 13 (h), the local equivalent plastic strain is mostly concentrated at the α grain boundaries (Figure 14 (f)), while the plastic strain is more evenly distributed within the interior of α grains. This is because the mixed microstructure with α variants and β matrix is included in the modified Hall-Petch relationship (Eq. (26a)). Hence, the local equivalent plastic strain is higher around the interfacial region between α variants and β matrix, which would be the reason that small cracks are initiated around grain boundaries [30]. Similar to the simulation in Figure 9 (a), the effect of external tensile load is more obvious than the consideration of plastic deformation and strain hardening, cf. Figure 14 (d). The selected areas imply the different effect of tensile load on MT for different parent β grains, but the effect is relatively complex due to the different grain size, shape and crystallographic orientation [31, 33, 59].

The volume fraction of variants in different simulation conditions are shown in Figure 15 and Figure 16. The volume fractions of different variants from different parent grains (cf. Figure 15) indicate clearly the influence of applied condition on the formation of the microstructure. But different from Shi and Wang [16, 35], in the present work the total volume fractions of variant 1 and 2 within 16 parent grains remains almost the same with different conditions, which is consistent with Malik [60]. Because of the small plastic deformation relaxation and simulation time, ~30% β matrix is retained, but with proper plastic kinetic coefficient and boundary condition, the MT should be finished without β matrix in microstructure within the delay considered here [62].

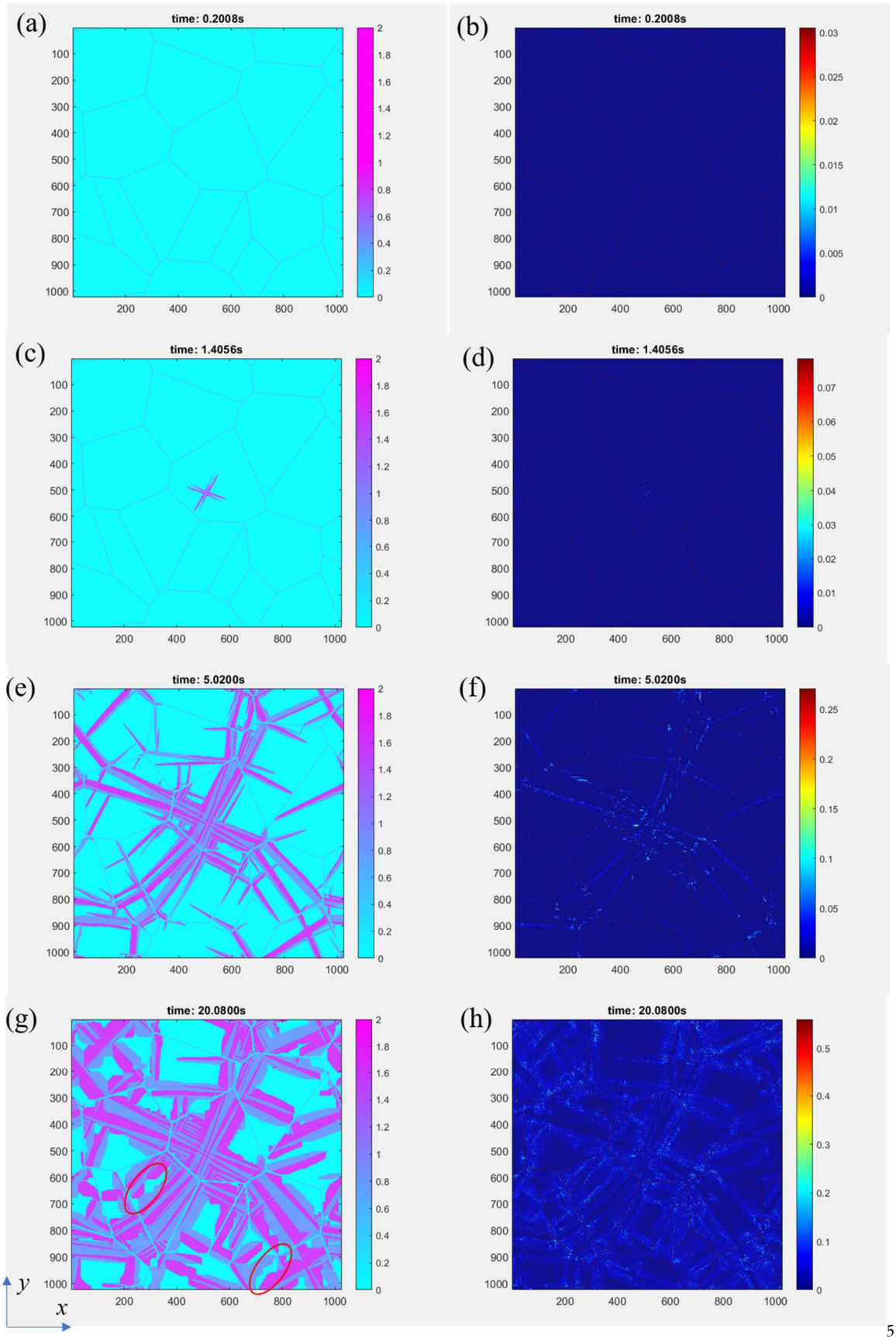

Figure 13. The microstructure and distribution of equivalent plastic strain with plastic deformation.

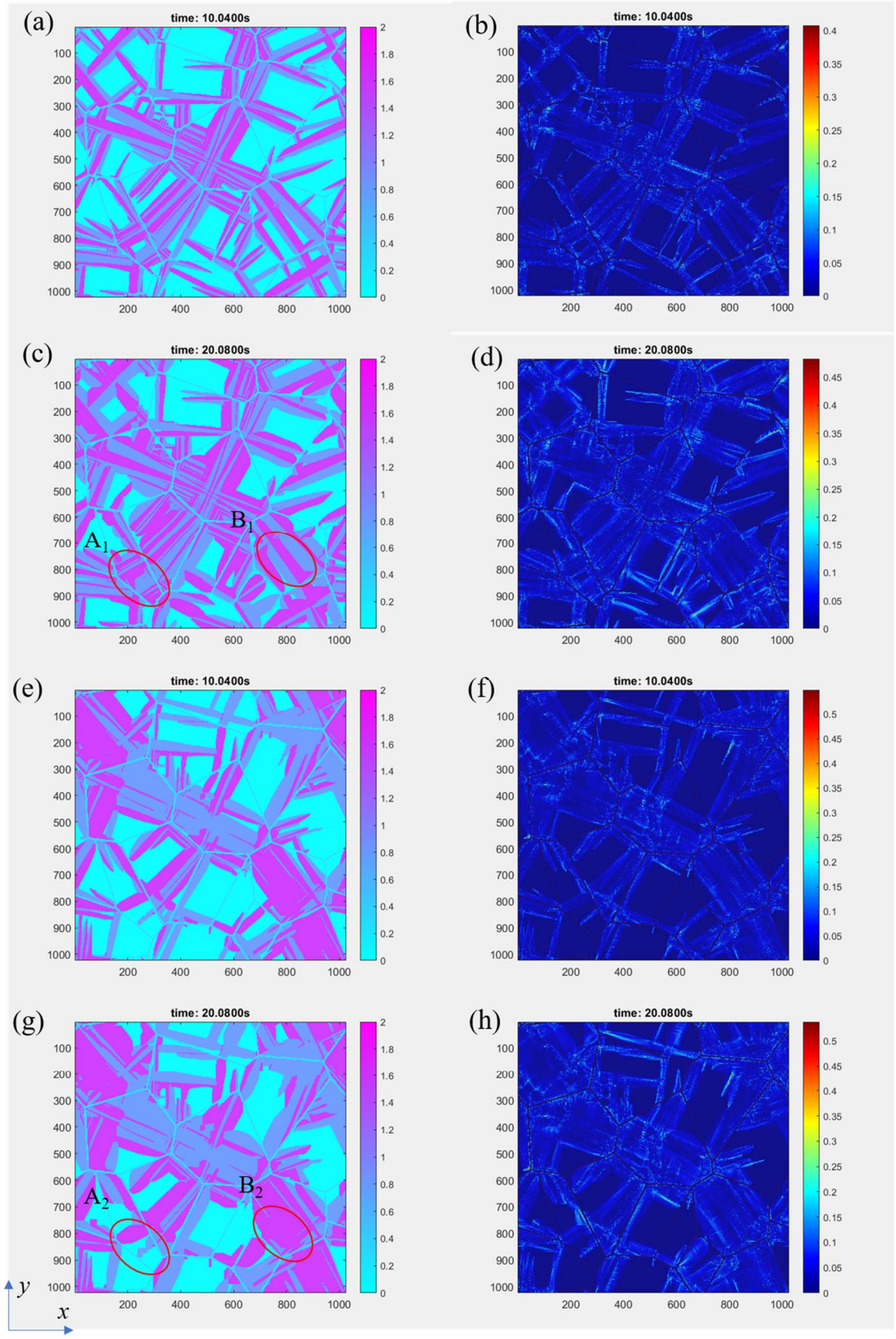

Figure 14. The microstructure and distribution of equivalent plastic strain with plastic deformation, strain hardening and tensile stress: (a)~ (d): plastic deformation and strain hardening; (e)~ (h): plastic deformation, strain hardening and tensile stress.

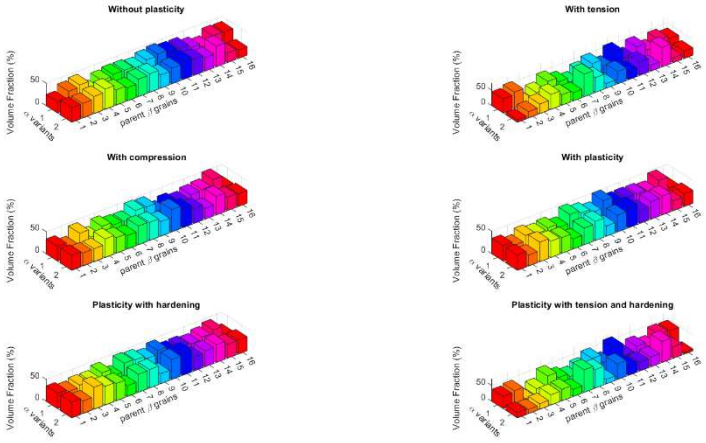

Figure 15. The volume fraction of variant 1 and 2 from different parent grains for different simulations.

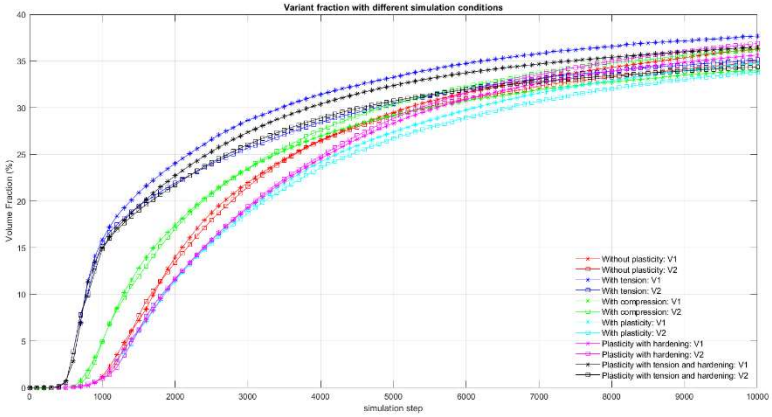

Figure 16. The total volume fraction of variant 1 and 2 for different simulations.

5. Conclusions

In the current work, phase field modelling is employed to study the microstructure evolution during phase transformation in Ti64 alloy under different conditions. It is concluded that the nucleation and growth of product α variants during martensitic transformation can be predicted in 2D and 3D dimensions, the local strain and stress distribution can be calculated.

In terms of nucleation at grain boundaries, the results allow to conclude that the grain boundary plays a key role through partially relaxing the transformation strain during MT, and the simulation of variant nucleation is consistent with observed nucleation event. The external loading can favor the occurrence of new variants at grain boundaries, but the effect of applied compressive stress is more obvious at triple junction points.

Regarding the plastic deformation during martensite growth, the relaxation of plastic strain should be considered, which induces coarsening of variants. The relatively large plastic strain can favor the MT procedure by reducing the local elastic strain. The external loading interacts with the local strain and induces the nucleation of variants through decreasing the local elastic strain energy, but for different parent grains with different orientations, the effect is different.

Supplementary Materials: Video S1: microstructure evolution of nucleation of 2 variants without external loading in 2D; Video S2: microstructure evolution of nucleation of 2 variants with applied compressive stress in 2D; Video S3: microstructure evolution of nucleation of 2 variants with applied tensile stress in 2D; Video S4: microstructure evolution of variants growth without plastic deformation in 2D; Video S5: microstructure evolution of variants growth with plastic deformation, strain

hardening and applied tensile stress in 2D; Video S6: microstructure evolution of variants growth without plastic deformation, strain hardening or applied tensile stress in 3D;

Author Contributions: Conceptualization, methodology, software, H. Xiang; writing—original draft preparation, H. Xiang writing—review and editing, L. A.I. Kestens and W. Van Paepegem; supervision, L. A.I. Kestens and W. Van Paepegem; All authors have read and agreed to the published version of the manuscript.

Funding: This research received no external funding by the China Scholarship Council (No. 201706370021.

Institutional Review Board Statement: Not applicable.

Informed Consent Statement: Not applicable.

Data Availability Statement: the program of phase field modelling can be found through the link.

Conflicts of Interest: The authors declare no conflict of interest.

References

1. Kozłowska, A., Grajcar, A., Radwański, K., Opara, J., Matus, K. and Nuckowski, P.M., Microstructure and temperature-dependent mechanical behavior of hot-rolled TRIP-assisted microalloyed steel. *Mater. Charact.*, **2022**, *186*, pp.111804, DOI: 10.1016/j.matchar.2022.111804.
2. Wang, X. and Chou, K., EBSD study of beam speed effects on Ti-6Al-4V alloy by powder bed electron beam additive manufacturing. *J. Alloys Compd.*, **2018**, *748*, pp.236-244, DOI: 10.1016/j.jallcom.2018.03.173.
3. Otsuka, K. and Ren, X., Physical metallurgy of Ti–Ni-based shape memory alloys. Progress in materials science, 2005, 50, pp.511-678, DOI: 10.1016/j.pmatsci.2004.10.001.
4. Oh, Y.M., Jeong, Y.H., Lee, K.J. and Kim, S.J., Effect of various alloying elements on the martensitic transformation in Zr–0.8 Sn alloy. *J. Alloys Compd.*, **2000**, *307*, pp.318-323, DOI: 10.1016/S0925-8388(00)00871-9.
5. Bhattacharya, K., Conti, S., Zanzotto, G. and Zimmer, J., Crystal symmetry and the reversibility of martensitic transformations. *Nature*, **2004**, *428*, pp.55-59, DOI: 10.1038/nature02378.
6. Pond, R.C., Celotto, S. and Hirth, J.P., A comparison of the phenomenological theory of martensitic transformations with a model based on interfacial defects. *Acta. Mater*, **2003**, *51*, pp.5385-5398. DOI: 10.1016/S1359-6454(03)00395-1.
7. Bhadeshia, H.K.D.H., Worked examples in the geometry of crystals. Institute of Metals, 2006.
8. Smith, D.A. and Pond, R.C., Bollmann's O-Iattice theory; a geometrical approach to interface structure. *Int. Met. Rev.*, **1976**, *21*, pp.61-74, DOI: 10.1179/imtr.1976.21.1.61.
9. Khachaturyan, A. G.; Shatalov, G. A. Elastic energy of heterophase systems of lamellar inclusions. Physics of Metals and Metallography 1971, 31, 1-5.
10. Khachaturyan, A. G. Theory of Structural Transformations in Solids. John Wiley & Sons: New York, USA, 1983.
11. Chen, L.Q., Phase-field models for microstructure evolution. *Annu. Rev. Mater. Res.*, **2002**, *32*(1), pp.113-140. DOI: 10.1146/annurev.matsci.32.112001.132041.
12. Mamivand, M., Zaeem, M.A. and El Kadiri, H., A review on phase field modeling of martensitic phase transformation. *Comput. Mater. Sci.*, **2013**. 77, pp.304-311. DOI: 10.1016/j.commatsci.2013.04.059.
13. Moelans, N., Blanpain, B. and Wollants, P., An introduction to phase-field modeling of microstructure evolution. *Calphad*, **2008**, 32(2), pp.268-294. DOI: 10.1016/j.calphad.2007.11.003.
14. Wang, Y. and Khachaturyan, A.G., Three-dimensional field model and computer modeling of martensitic transformations. *Acta Mater*, **1997**, *45*, pp.759-773, DOI: 10.1016/S1359-6454(96)00180-2.
15. Jin, Y.M., Artemev, A. and Khachaturyan, A.G., Three-dimensional phase field model of low-symmetry martensitic transformation in polycrystal: simulation of ζ′ 2 martensite in AuCd alloys. *Acta Mater*, **2001**, *49*, pp.2309-2320, DOI: 10.1016/S1359-6454(01)00108-2.
16. Shi, R., Zhou, N., Niezgoda, S.R. and Wang, Y., Microstructure and transformation texture evolution during α precipitation in polycrystalline α/β titanium alloys–a simulation study. *Acta Mater*, **2015**, *94*, pp.224-243, DOI: 10.1016/j.actamat.2015.04.050.
17. Shen, C. and Wang, Y., Incorporation of γ-surface to phase field model of dislocations: simulating dislocation dissociation in fcc crystals. *Acta Mater*, **2004**, *52*, pp.683-691, DOI: 10.1016/j.actamat.2003.10.014.
18. Qiu, D., Shi, R., Zhang, D., Lu, W. and Wang, Y., Variant selection by dislocations during α precipitation in α/β titanium alloys. *Acta Mater*, **2015**, *88*, pp.218-231, DOI: 10.1016/j.actamat.2014.12.044.
19. Qiu, D., Shi, R., Zhao, P., Zhang, D., Lu, W. and Wang, Y., Effect of low-angle grain boundaries on morphology and variant selection of grain boundary allotriomorphs and Widmanstätten side-plates. *Acta Mater*, **2016**, *112*, pp.347-360, DOI: 10.1016/j.actamat.2016.04.033.
20. Wang, Y.U., Jin, Y.M. and Khachaturyan, A.G., Phase field microelasticity theory and modeling of elastically and structurally inhomogeneous solid. *Int. J. Appl. Phys.*, **2002**, *92*, pp.1351-1360, DOI: 10.1063/1.1492859.
21. Hu, S.Y. and Chen, L.Q., A phase-field model for evolving microstructures with strong elastic inhomogeneity. *Acta. Mater*, **2001**, *49*, pp.1879-1890, DOI: 10.1016/S1359-6454(01)00118-5.

22. Yu, P., Hu, S.Y., Chen, L.Q. and Du, Q., An iterative-perturbation scheme for treating inhomogeneous elasticity in phase-field models. Journal of Computational Physics, 2005, 208, pp.34-50, DOI: 10.1016/j.jcp.2005.02.015.
23. Bhattacharyya, S., Heo, T.W., Chang, K. and Chen, L.Q., A spectral iterative method for the computation of effective properties of elastically inhomogeneous polycrystals. *Commun. Comput. Phys*, **2012**, *11*, pp.726-738, DOI: 10.4208/cicp.290610.060411a.
24. Heo, T.W., Colas, K.B., Motta, A.T. and Chen, L.Q., A phase-field model for hydride formation in polycrystalline metals: Application to δ-hydride in zirconium alloys. *Acta Mater*, **2019**, *181*, pp.262-277, DOI: 10.1016/j.actamat.2019.09.047.
25. Hu, X., Ji, Y., Heo, T.W., Chen, L.Q. and Cui, X., Phase-field model of deformation twin-grain boundary interactions in hexagonal systems. *Acta Mater*, **2020**, *200*, pp.821-834, DOI: 10.1016/j.actamat.2020.09.062.
26. Guo, X.H., Shi, S.Q. and Ma, X.Q., Elastoplastic phase field model for microstructure evolution. *Appl. Phys. Lett*, **2005**, *87*, pp.221910, DOI: 10.1063/1.2138358.
27. Yamanaka, A., Takaki, T. and Tomita, Y., Elastoplastic phase-field simulation of self-and plastic accommodations in cubic→ tetragonal martensitic transformation. *Mater. Sci. Eng. A*, **2008**, *491*, pp.378-384, DOI: 10.1016/j.msea.2008.02.035.
28. Yamanaka, A., Takaki, T. and Tomita, Y., Elastoplastic phase-field simulation of martensitic transformation with plastic deformation in polycrystal. *Int. J. Mech. Sci.*, **2010**, *52*, pp.245-250, DOI: 10.1016/j.ijmecsci.2009.09.020.
29. Yeddu, H.K., Malik, A., Ågren, J., Amberg, G. and Borgenstam, A., Three-dimensional phase-field modeling of martensitic microstructure evolution in steels. *Acta Mater*, **2012**, *60*, pp.1538-1547, DOI: 10.1016/j.actamat.2011.11.039.
30. Malik, A., Yeddu, H.K., Amberg, G., Borgenstam, A. and Ågren, J., Three dimensional elasto-plastic phase field simulation of martensitic transformation in polycrystal. *Mater. Sci. Eng. A*, **2012**, *556*, pp.221-232, DOI: 10.1016/j.msea.2012.06.080.
31. Yeddu, H.K., Phase-field modeling of austenite grain size effect on martensitic transformation in stainless steels. *Comput. Mater. Sci.*, **2018**, *154*, pp.75-83, DOI: 10.1016/j.commatsci.2018.07.040.
32. Jang, D. and Atzmon, M., Grain-boundary relaxation and its effect on plasticity in nanocrystalline Fe. *Int. J. Appl. Phys.*, **2006**, *99*, pp.083504, DOI: 10.1063/1.2187417.
33. Heo, T.W. and Chen, L.Q., Phase-field modeling of displacive phase transformations in elastically anisotropic and inhomogeneous polycrystals. *Acta Mater*, **2014**, *76*, pp.68-81, DOI: 10.1016/j.actamat.2014.05.014.
34. Shi, R. and Wang, Y., Variant selection during α precipitation in Ti–6Al–4V under the influence of local stress–A simulation study. *Acta Mater*, **2013**, *61*, pp.6006-6024, DOI: 10.1016/j.actamat.2013.06.042.
35. Zhang, J., Li, X., Xu, D., Teng, C., Wang, H., Yang, L., Ju, H., Xu, H., Meng, Z., Ma, Y. and Wang, Y., Phase field simulation of the stress-induced α microstructure in Ti–6Al–4 V alloy and its CPFEM properties evaluation. *J Mater Sci Technol*, **2021**, *90*, pp.168-182, DOI: 10.1016/j.jmst.2020.12.085.
36. Perrin, J.,Mouvement brownien et réalité moléculaire. *1909*.
37. Petschek, R.G. and Metiu, H., A computer simulation of the time-dependent Ginzburg–Landau model for spinodal decomposition. *J. Chem. Phys*., **1983**, *79*, pp.3443-3456, DOI: 10.1063/1.446194.
38. Rogers, T.M., Elder, K.R. and Desai, R.C., Numerical study of the late stages of spinodal decomposition. *Phys. Rev. B*., **1988**, *37*, pp.9638, DOI: 10.1103/PhysRevB.37.9638.
39. Olson, G.B., Cohen, M. A general mechanism of martensitic nucleation: Part II. FCC → BCC and other martensitic transformations. *Metall Mater Trans A*, **1976**, *7*, pp.1905–1914, DOI: 10.1007/BF02659823.
40. Ueland, S.M. and Schuh, C.A., Grain boundary and triple junction constraints during martensitic transformation in shape memory alloys. *Int. J. Appl. Phys.*, **2013**, *114*, p.053503, DOI: 10.1063/1.4817170.
41. Ueda, M., Yasuda, H.Y. and Umakoshi, Y., Controlling factor for nucleation of martensite at grain boundary in Fe-Ni bicrystals. *Acta Mater*, **2003**, *51*, pp.1007-1017, DOI: 10.1016/S1359-6454(02)00503-7.
42. Tan, X., Kok, Y., Toh, W. et al. Revealing martensitic transformation and α/β interface evolution in electron beam melting three-dimensional-printed Ti-6Al-4V. *Sci Rep*, **2016**, *6*, pp.26039, DOI: 10.1038/srep26039.
43. Kim, J., Kim, KH. & Kwon, D. Evaluation of high-temperature tensile properties of Ti-6Al-4V using instrumented indentation testing. *Met. Mater. Int*. **2016**, *22*, pp.209–215, DOI: 10.1007/s12540-016-5619-3.
44. Li, P.H., Guo, W.G., Huang, W.D., Su, Y., Lin, X. and Yuan, K.B., Thermomechanical response of 3D laser-deposited Ti–6Al–4V alloy over a wide range of strain rates and temperatures. *Mater. Sci. Eng. A*, **2015**, *647*, pp.34-42, DOI: 10.1016/j.msea.2015.08.043.
45. Galindo-Fernández, M.A., Mumtaz, K., Rivera-Diaz-del-Castillo, P.E.J., Galindo-Nava, E.I. and Ghadbeigi, H., A microstructure sensitive model for deformation of Ti-6Al-4V describing Cast-and-Wrought and Additive Manufacturing morphologies. *Mater. Des.*, **2018**, *160*, pp.350-362, DOI: 10.1016/j.matdes.2018.09.028.
46. Hou, X., Liu, Z., Wang, B., Lv, W., Liang, X. and Hua, Y., 2018. Stress-strain curves and modified material constitutive model for Ti-6Al-4V over the wide ranges of strain rate and temperature. *Materials*, **2018**, *11*, pp.938, DOI: 10.3390/ma11060938.
47. López, J.G., Verleysen, P., Naghdy, S. and Kestens, L.A., Comparison of the Johnson-Cook and VPSC models to describe the constitutive behaviour of Ti-6Al-4V in an implicit finite element scheme. *Key Eng. Mater*, **2015**, *651*, pp.564-569, DOI: 10.4028/www.scientific.net/KEM.651-653.564.
48. Lindwall, G., Moon, K.W., Chen, Z., Mengason, M., Williams, M.E., Gorham, J.M., Zhao, J.C. and Campbell, C.E., Diffusion in the Ti-Al-V system. J. Ph. Equilibria Diffus., 2018, 39, pp.731-746, DOI: 10.1007/s11669-018-0673-9.
49. Welsch, G., Boyer, R. and Collings, E.W. eds., Materials properties handbook: titanium alloys. *ASM international*. **1993**.
50. Stanford, N. and Bate, P.S., Crystallographic variant selection in Ti–6Al–4V. *Acta Mater*, **2004**, *52*, pp.5215-5224, DOI: 10.1016/j.actamat.2004.07.034.
51. Lavogiez, C., Dancette, S., Cazottes, S., Le Bourlot, C. and Maire, E., In situ analysis of plasticity and damage nucleation in a Ti-6Al-4V alloy and laser weld. *Mater. Charact.*, **2018**, *146*, pp.81-90, DOI: 10.1016/j.matchar.2018.09.039.

52. Liu, J., Zhang, K., Yang, Y., Wang, H., Zhu, Y. and Huang, A., Grain boundary α-phase precipitation and coarsening: Comparing laser powder bed fusion with as-cast Ti-6Al-4V. *Scr. Mater.*, **2022**, *207*, pp.114261, DOI: 10.1016/j.scriptamat.2021.114261.
53. Qiu, D., Zhao, P., Shi, R., Wang, Y. and Lu, W., 2016. Effect of autocatalysis on variant selection of α precipitates during phase transformation in Ti-6Al-4V alloy. *Comput. Mater. Sci.*, **2016**, *124*, pp.282-289, DOI: 10.1016/j.commatsci.2016.07.032.
54. Xu, G., Wang, C., Beltrán, J.I., LLorca, J. and Cui, Y., Landau modeling of dynamical nucleation of martensite at grain boundaries under local stress. *Comput. Mater. Sci.*, **2016**, *118*, pp.103-111, DOI: 10.1016/j.commatsci.2016.02.042.
55. Jones, D.R., Fensin, S.J., Dippo, O., Beal, R.A., Livescu, V., Martinez, D.T., Trujillo, C.P., Florando, J.N., Kumar, M. and Gray III, G.T., Spall fracture in additive manufactured Ti-6Al-4V. *Int. J. Appl. Phys.*, **2016**, *120*, pp.135902, DOI: 10.1063/1.4963279.
56. Davis, A.E., Donoghue, J., Kennedy, J.R., Byres, N. and Prangnell, P.B., In-situ observation of single variant α colony formation in Ti-6Al-4V. *Acta Mater*, **2021**, *220*, pp.117315, DOI: 10.1016/j.actamat.2021.117315.
57. Kestens, L., Petrov, R. and Houbaert, Y., Orientation selective martensite transformation in an Fe-28Ni alloy. *ISIJ Int*, **2003**, *43*, pp.1444-1452, DOI: 10.2355/isijinternational.43.1444.
58. Cui, S., Cui, Y., Wan, J., Rong, Y. and Zhang, J., Grain size dependence of the martensite morphology–a phase-field study. *Comput. Mater. Sci.*, **2016**, *121*, pp.131-142, DOI: 10.1016/j.commatsci.2016.05.007.
59. Van Bohemen, S.M.C., Kamp, A., Petrov, R.H., Kestens, L.A.I. and Sietsma, J., Nucleation and variant selection of secondary α plates in a β Ti alloy. *Acta Mater*, **2008**, *56*, pp.5907-5914, DOI: 10.1016/j.actamat.2008.08.016.
60. Malik, A., Amberg, G., Borgenstam, A. and Ågren, J., Effect of external loading on the martensitic transformation–A phase field study. *Acta Mater*, **2013**, *61*, pp.7868-7880, DOI: 10.1016/j.actamat.2013.09.025.
61. Ali, T., Wang, L., Cheng, X., Cheng, H., Yang, Y., Liu, A., Xu, X., Zhou, Z., Ning, Z., Xu, Z. and Min, X., Mechanical (compressive) form of driving force triggers the phase transformation from β to ω & α''phases in metastable β phase-field Ti-5553 alloy. *J Mater Sci Technol*, **2021**, *78*, pp.238-246, DOI: 10.1016/j.jmst.2020.11.033.
62. Zhang, X., Shen, G., Xu, J. et al. Analysis of Martensitic Transformation Plasticity Under Various Loadings in a Low-Carbon Steel: An Elastoplastic Phase Field Study. *Metall Mater Trans A*, **2020**, *51*, pp.4853–4867, DOI: 10.1007/s11661-020-05889-9.